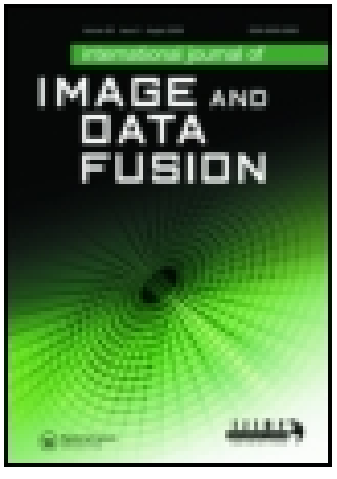

International Journal of Image and Data Fusion
Publication details, including instructions for authors and subscription information:
http://www.tandfonline.com/loi/tidf20

Ground deformation mapping by fusion of multi-temporal interferometric synthetic aperture radar images: a review

Lei Zhang[a], Xiaoli Ding[a] & Zhong Lu[b]
[a] Land Surveying and Geoinformatics, The Hong Kong Polytechnic University, Kowloon, Hong Kong
[b] Roy M. Huffington Department of Earth Sciences, Southern Methodist University, Dallas, Texas, USA
Published online: 30 Jul 2015.

To cite this article: Lei Zhang, Xiaoli Ding & Zhong Lu (2015): Ground deformation mapping by fusion of multi-temporal interferometric synthetic aperture radar images: a review, International Journal of Image and Data Fusion, DOI: 10.1080/19479832.2015.1068874

To link to this article: http://dx.doi.org/10.1080/19479832.2015.1068874

International Journal of Image and Data Fusion, 2015
http://dx.doi.org/10.1080/19479832.2015.1068874

Taylor & Francis
Taylor & Francis Group

REVIEW ARTICLE

Ground deformation mapping by fusion of multi-temporal interferometric synthetic aperture radar images: a review

Lei Zhang[a]*, Xiaoli Ding[a] and Zhong Lu[b]

[a]*Land Surveying and Geoinformatics, The Hong Kong Polytechnic University, Kowloon, Hong Kong;*
[b]*Roy M. Huffington Department of Earth Sciences, Southern Methodist University, Dallas, Texas, USA*

(*Received 9 December 2014; accepted 19 June 2015*)

Interferometric synthetic aperture radar (InSAR) has emerged as a powerful geodetic imaging technique in the past two decades, focused on the retrieval of deformation, topography and even meteorological measurements by the analysis of phase components of complex-valued radar data. The strength of this technique lies in its abilities of all-weather, day and night data acquisition, high measurement accuracy and wide spatial scale. Although vast successful applications have been achieved, conventional InSAR technique possesses several limitations (e.g. decorrelation, phase unwrapping error and atmospheric artefacts), which, in turn, have motivated the development of advanced multi-temporal InSAR (MTInSAR) analysis techniques. Fusion of MTInSAR imagery of the same area has led to a marked improvement in the reliability and accuracy of derived products (e.g. deformation) and has also been important for gleaning dynamic signals of deformation over a wide range of temporal scales. This paper is intended to introduce the development of MTInSAR and provide a practical guidance to the users of the technique. Specially, cross-comparison among approaches employed by different MTInSAR techniques is conducted using either simulated or real datasets. We have addressed the weakness of each approach and highlighted the potential technical improvement.

Keywords: InSAR; deformation monitoring; multi-temporal analysis

1. Introduction

Interferometric synthetic aperture radar (InSAR) can provide measurements of deformation along the radar line of sight (LOS) with centimetre to millimetre level of accuracy and paramount resolution by exploiting the phase differences between two temporally separated synthetic aperture radar (SAR) images over an area of interest (Gabriel *et al*. 1989). The past two decades have witnessed InSAR's unique abilities in addressing the needs and answering the questions that classic optical remote sensing techniques have been unable or difficult to tackle. Vast applications have been achieved in studying and monitoring natural and anthropological hazards ranging from volcano (e.g. Hooper *et al*. 2007, Lu *et al*. 2010), earthquake (e.g. Simons *et al*. 2002, Feng *et al*. 2010, Hu *et al*. 2012), landslide (e.g. Hilley *et al*. 2004, Zhao *et al*. 2012, Sun *et al*. 2015), urban ground deformation (e.g. Fruneau and Sarti 2000; Zhang *et al*. 2012), to infrastructure monitoring (e.g. Thiele *et al*. 2007, Reale *et al*. 2011, Chang and Hanssen 2014). However, onerous challenges imposed by spatial–temporal decorrelation of radar signals, atmospheric artefacts and aliasing of long-wavelength deformation and orbit ramps have demanded the

*Corresponding author. Email: lslzhang@polyu.edu.hk

improvement on the performance of conventional InSAR method. Since Usai and Hanssen (1997) first suggested that useful information can be retrieved from pixels that keep high coherence for a long period, it has been demonstrated that the enhancement can be achieved by the fusion of multi-temporal SAR data, which makes full exploitation of the inherent information from radar returns. Over the years, abundant techniques involving the joint analysis of a set of SAR images have been proposed and denoted by different names, for example permanent scatterer InSAR (PSInSAR) (Ferretti *et al*. 2001), persistent scatterer interferometry (PSI) (e.g. Adam *et al*. 2009, Crosetto *et al*. 2010), small baseline subset (SBAS) technique (Berardino *et al*. 2002, Lanari *et al*. 2004), Stanford method for persistent scatterers (StaMPS) (Hooper *et al*. 2004), spatial–temporal unwarpping network (STUN) algorithm (Kampes 2006), coherent point target (CPT) technique (Mora *et al*. 2003), interferometric point target analysis (IPTA) (Werner *et al*. 2003) and temporarily coherent point InSAR (TCPInSAR) (Zhang *et al*. 2011). All these techniques have the ability to overcome (at least partially) the weaknesses of conventional InSAR.

Although the detailed implementations of these multi-temporal InSAR (MTInSAR) techniques vary from one to the other, their technical innovations mainly lie in three common aspects: observation selection, modelling and parameter estimation. High-quality observations are always desired for any MTInSAR technique, which leads to an emphasis on identifying points (pixels in the SAR imagery) with little decorrelation from the interferogram stacks generated based on the framework of either single-master or multiple-master approach. Taking these points as observations can significantly reduce the noise term of interferometric phase, and by differencing among neighbouring points, a point network consisting of numerous arcs is constructed, where the spatially correlated atmospheric component can be further reduced. Once the observations (either the phases at points or the phase differences at arcs) have been fixed, modelling, that is construction of observation function that reflects the relationship between the observation and parameters is closely followed. Parameters that can be modelled include the topography residuals, look angle error, the orbit inaccuracy, height-related atmospheric artefacts and deformation time series. Provided that linear deformation is assumed, the deformation rate can also be modelled. It is worth noting that although it is possible to simultaneously model all parameters, efficient and reliable solver for such an underdetermined observation system might not be available. Therefore among current MTInSAR techniques, one strategy that has been widely adopted is to separate the deformation term from other parameters first and then retrieve the full resolution deformation time series. Once the observation function is built up, the following step is to estimate the parameters. In this step, whether the observations contain phase ambiguities determines the complexity of solvers. For the unwrapped observations, the least squares method (Usai 2003) or minimum-norm least squares (Berardino *et al*. 2002, Casu *et al*. 2006) is sufficient to serve as a parameter solver. Instead of using the minimum-norm criteria, Laplacian smoothing can also be used for an observation system with rank deficiency (Schmidt and Bürgmann 2003, Wang *et al*. 2012). To suppress the effect of unwrapping error, robust L-1 norm solver (Lauknes *et al*. 2011) has been recently suggested. However, for the wrapped observations, direct solution is usually obscure. In fact there have been a huge flurry of efforts on this over the years. Methods such as ensemble coherence maximisation (Ferretti *et al*. 2001, Colesanti *et al*. 2003), integer least squares (Kampes and Hanssen 2004), 3D phase unwrapping (Hooper *et al*. 2004, 2007) and least squares with ambiguity detector (Zhang *et al*. 2011, 2012, 2014) have been proposed and achieved with many successful applications. With the solvers, deformation signal can be retrieved form either wrapped or

unwrapped interferometric phases, however there is an intractable error hindering an accurate estimation of deformation time series. This error is caused by atmospheric turbulence, which has a varying spatial correlation and a similar temporal behaviour to the nonlinear deformation in some cases (Hanssen 2001, Li *et al*. 2005, Ding *et al*. 2008, Jolivet *et al*. 2014). Spatial–temporal filtering (Ferretti *et al*. 2001, Berardino *et al*. 2002, Hooper *et al*. 2004, Gong *et al*. 2015) whose performance largely depends on the operators' experience, although not robust enough, has been widely used to eliminate this kind of error.

The purpose of this paper is to provide a comprehensive overview to understanding the essential features of approaches used in the aforementioned three aspects. It is organised as follows. We begin with a brief introduction of limitations associated with conventional InSAR technique (Section 2), which actually motivated the development of MTInSAR techniques. We then focus on the analysis of the advantages and disadvantages of observations employed by current MTInSAR techniques. The modelling that links the unknowns and phase observations is described in Section 3. The parameter estimators are introduced in Section 4 where a comparison between four estimators using Environmental Satellite (Envisat)/advanced synthetic aperture radar (ASAR) data over east coastal zone of Taiwan is also conducted. Finally in Section 5 we summarise the development of current MTInSAR techniques and suggest some directions for future research.

2. Inherent limitations of conventional InSAR

To understand the development of MTInSAR and appreciate its unique advantages, it is imperative to understand limitations associated with conventional InSAR and how these limitations affect the accuracy of the retrieved deformation. It should be noted that these limitations do not undermine the importance of conventional InSAR method which is still being used to retrieve large and sudden deformation signals such as those associated with large earthquakes, volcano eruptions and landslides.

Let us start from a stack of differential InSAR images where the phase contribution raised by topography has been largely eliminated by external digital elevation model (DEM) (e.g. shuttle radar topography mission (SRTM) and advanced space-borne thermal emission and reflection radiometer (ASTER) DEM). Given a pixel with the location index (x) in the ith interferogram, the wrapped differential phase ($\phi^i_{\mathrm{dint},x}$) usually includes five contributions, that is

$$\phi^i_{\mathrm{dint},x} = W\left\{-\frac{4\pi}{\lambda}\left(d^i_{\mathrm{los},x}+\frac{\mathrm{B}^i_{\perp,x}\,h_{\mathrm{res},x}}{R_x\sin\theta_x}\right)+\phi^i_{\mathrm{atm},x}+\phi^i_{\mathrm{orb},x}+\phi^i_{n,x}\right\} \tag{1}$$

where λ is the radar wavelength, R_x the slant range distance, θ_x the radar look angle, $B^i_{\perp,x}$ the perpendicular baseline, $d^i_{\mathrm{los},x}$ the surface deformation projected to the radar LOS direction, $h_{\mathrm{res},x}$ the topographic inaccuracy, $\phi^i_{\mathrm{atm},x}$ the phase artefact due to the difference in atmospheric retardation between passes, $\phi^i_{\mathrm{orb},x}$ the phase residual raised by orbit errors, $\phi^i_{\mathrm{n},x}$ a noise term resulting from temporal/geometry decorrelation and other noise sources and $W\{\cdot\}$ the wrapping operator. If the deformation ($d^i_{\mathrm{los},x}$) is the signal of our interest, the remaining terms are then the error sources. These errors limit the accuracy of conventional InSAR-derived deformation. The main purpose of MTInSAR techniques is to eliminate or reduce these errors, therefore understanding the spatial and temporal characteristics of these errors is vital. Among these errors, topographic error is caused by DEM inaccuracy,

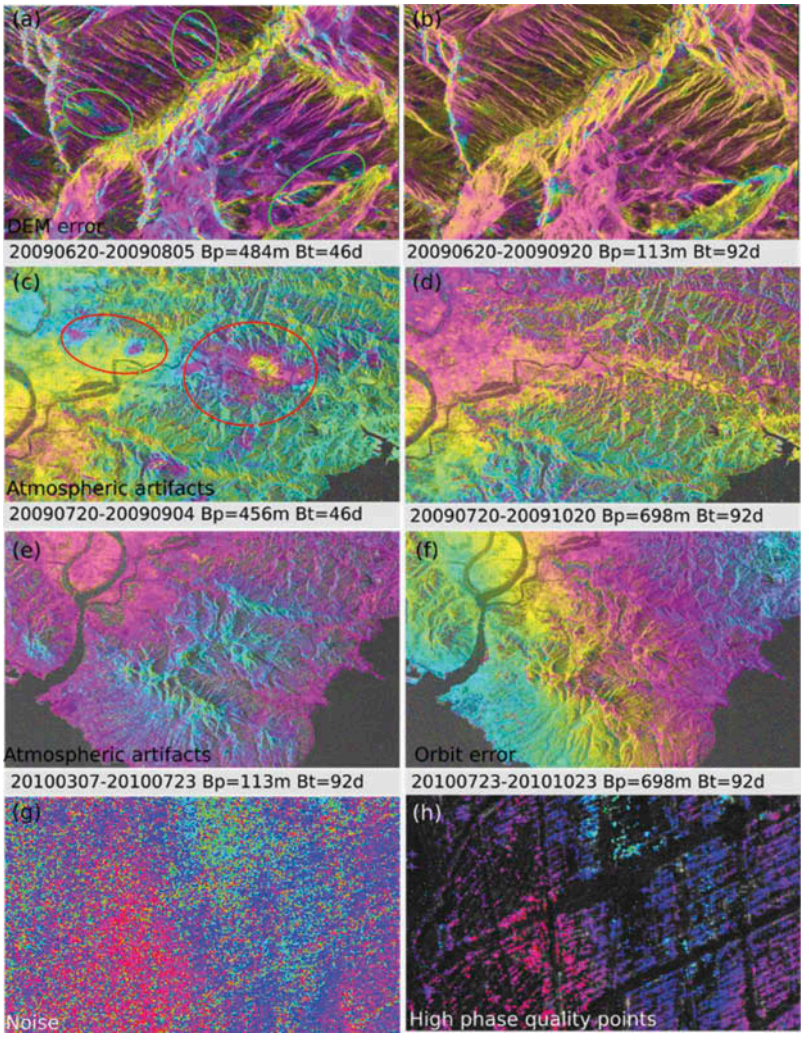

Figure 1. Error sources associated with conventional InSAR measurements: (a) interferogram over a mountainous area with a relatively longer spatial baseline; (b) interferogram with a shorter spatial baseline. The comparison between (a) and (b) clearly indicates the effect of DEM error on InSAR measurements (e.g. the areas enclosed by circles in (a)). (c) Interferogram for the period of July–September 2009; (d) interferogram for the period of July–October 2009. By comparing (c) and (d), we can conclude patterns in circles in (c) are caused by atmospheric artefacts (i.e. TAA). (e) Interferogram containing patterns raised by SAA which is related to topography height; (f) orbit error in interferogram; (g) interferogram with heavy noise; (h) phases at HPQ points isolated from (g).

which could be spatially correlated or more likely uncorrelated. Equation (1) indicates that this error term has a definitive relationship with interferometric phase via the perpendicular baseline at a given pixel. Figure 1(a) and (b) show two phase images under different perpendicular baseline lengths, clearly indicating that the main phase anomalies in the circled areas in Figure 1(a) come from topographic error. However, when only one

interferogram is available, the topographic phase residual can be easily mistaken as deformation signal.

Atmospheric artefact is another error source that has not been well tackled in conventional InSAR technique and actually is also challenging for MTInSAR techniques. The atmospheric artefact is generated when radar microwave propagates twice through the atmosphere from SAR satellite to ground and back again. The variations in the refractive index along the propagation path inevitably introduce errors to InSAR measurements (Massonnet *et al.* 1994, Zebker *et al.* 1997, Lu and Dzurisin 2014). It is well known that the atmospheric artefact constitutes of phase variations caused by both ionosphere and troposphere. Compared with the ionosphere artefact, the troposphere anomaly is rather thornier due to its complicated spatial–temporal variations (Hanssen 2001, Lu and Dzurisin 2014). Troposphere artefacts in the InSAR measurements can further be decomposed into turbulent and stratified components (Hanssen 2001). Turbulent atmospheric artefact (TAA) is mainly induced by the high variability of water vapour contained in the near-ground troposphere, where a strong turbulent mixing process occurs. Localised phase gradient can be caused by TAA in both flat and mountainous regions, which usually mimics the surface deformation associated with, for example groundwater and landslides (Lu and Dzurisin 2014). Stratified atmospheric artefact (SAA) is the additional phase delay in mountainous regions induced by stratification of the atmosphere into different vertical refractivity layers. High correlation between SAA and topographic height can always be found (e.g. Remy *et al.* 2003, Biggs *et al.* 2007). Figure 1(c)–(e) give examples of these two typical artefacts. The comparison between Figure 1(c) and (e) indicates that the effect of TAA can behave very like deformation signals, raising risks for the application of conventional InSAR. TAA usually appears to be spatially correlated, with the correlation dimension ranging from metres to kilometres. On the other hand, TAA generally appears to be temporally uncorrelated, while in some cases it could also be seasonally variable (Hooper *et al.* 2007). TAA's unique spatial–temporal characteristics cause difficulties in an effective elimination. The essential gist is that it is difficult to separate the temporal fluctuation of TAA from non-linear deformation. InSAR is vulnerable to serious atmospheric artefacts, and this rather than phase decorrelation is its major technical handicap.

Orbit error is caused by inaccurate determination of satellite state vectors, behaving as long wavelength signal in interferograms. Figure 1(f) provides an example of orbit error. The phase related to orbit error can often be modelled and removed using a polynomial after the interferogram is successfully unwrapped. However this practice also has a risk, as a part of long-wavelength deformation signal might also be removed (Zhang *et al.* 2014). The noise error is mainly due to spatial–temporal decorrelation (Zebker and Villasenor 1992). Large deformation gradient can also introduce decorrelation. As an example, Figure 2 shows several interferograms over a reclaimed area in Hong Kong with increasing temporal intervals, where the decorrelation caused by rapid ground subsidence can be clearly observed. To reduce the noise term, one natural way is only selecting high phase quality (HPQ) points. The last error rests on the success rate of phase unwrapping associated with the conventional InSAR processing, which is mainly due to heavy decorrelation, large magnitude of deformation or unoptimised phase unwrapping strategy.

3. Observations of MTInSAR

We start the introduction of MTInSAR techniques from their observations, that is the interferogram stack by differencing multi-temporal SAR phase images. Interferograms can be formed by two different strategies. One is single-master approach where all

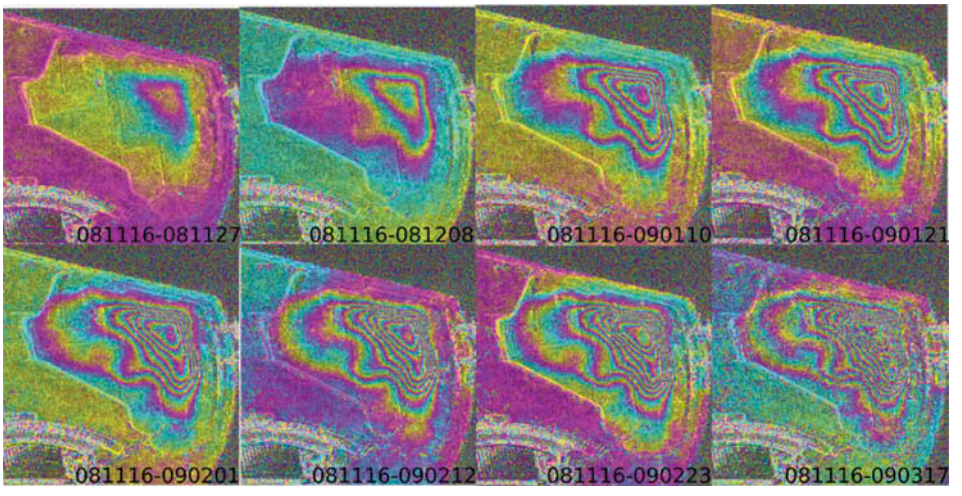

Figure 2. Interferograms with increasing temporal baselines. It is clear that rapid deformation can introduce serious decorrelation and make deformation retrieval impossible for single-master strategy.

interferograms are formed with respect to a single master (reference) image. The other is multi-master approach where interferograms consist of SAR pairs meeting certain spatial and/or temporal baseline thresholds. Both strategies are adopted by current MTInSAR techniques, while each possesses its own advantages and disadvantages. Single-master interferograms are generally considered to be optimal for DEM refinement since the length of perpendicular baselines has a large variance. However, long baseline raised by single-master construction strategy can introduce serious decorrelation, which can significantly reduce the number of HPQ points, and in extreme cases makes the deformation estimation impossible. Let us take Figure 2 again as an example. It shows a typical single-master interferogram stack. With the increase of temporal baseline, the fringe gradient is getting precipitous, finally resulting in serious decorrelation which hinders the retrieval of ground deformation. The multiple-master interferogram strategy appears to be rather flexible. By narrowing the baseline tube, the decorrelation can be well reduced, resulting in abundant HPQ points. However, the retrieved DEM error is not accurate and reliable as multiple-master interferograms are often constructed from short-baseline image pairs. For instance, Figure 3 depicts an accuracy comparison between the estimated DEM errors from four stacks of interferograms with different baselines. In these two cases, the DEM error is estimated together with coefficients of a predefined deformation model (i.e. a second-order polynomial), which is a typical routine of SBAS technique. In the case where the “true” (simulated) deformation is periodic (Figure 3(a)), we set 100 m and 745 days as the baseline thresholds to select a set of interferograms. From the selected interferograms, we then estimate the parameters mentioned above. Figure 3(b) shows the histogram of differences between the estimated DEM error and the “true” DEM error. We then extend the perpendicular baseline threshold to 220 m to include more interferograms as observations. The DEM error and deformation are resolved again from these observations. The differences with true DEM error are shown in Figure 3(c). Similarly, for the deformation having a fluctuant pattern (Figure 3(d)), we estimate the parameters from two sets of interferograms selected according to thresholds of 160 m/745 days and 220 m/745

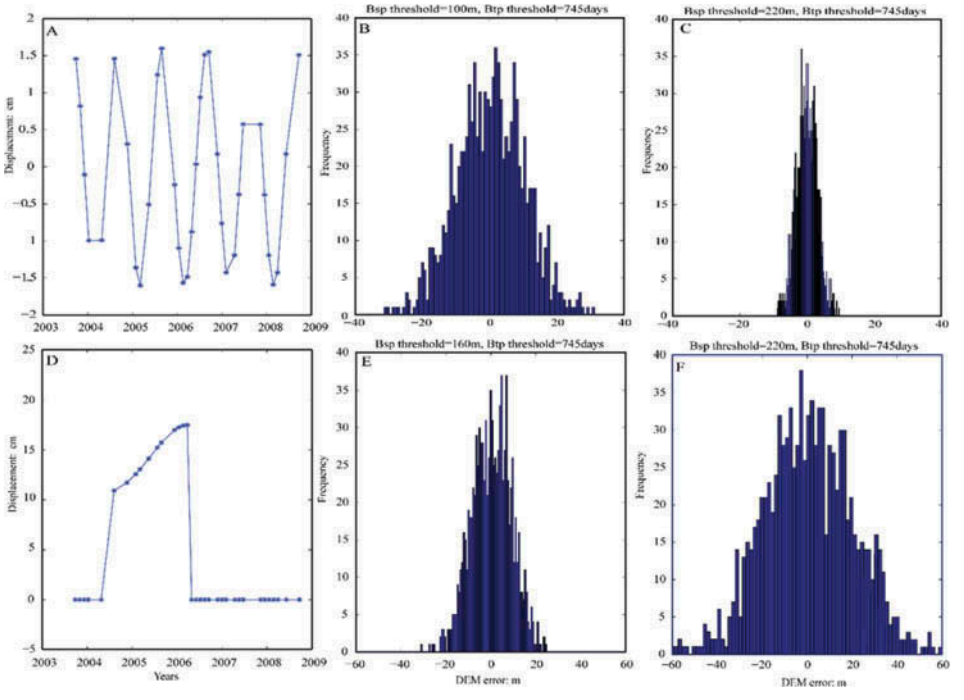

Figure 3. The effect of baseline threshold on the accuracy of the estimated DEM error: (a) simulated periodical deformation signal; (b) histogram of residuals of DEM error estimated from a set of simulated C-band interferograms with baseline thresholds of 100 m and 745 days; (c) histogram of residuals of DEM error with baseline thresholds of 220 m and 745 days; (d) simulated fluctuant deformation signal; (e) histogram of residuals of DEM error with baseline thresholds of 160 m and 745 days; (f) histogram of residuals of DEM error with baseline thresholds of 220 m and 745 days.

days, respectively. The corresponding histograms of residuals of DEM error are shown in Figure 3(e) and (f). The comparison among the residual histograms clearly indicates that an improper deformation model and unsuitable baseline threshold can introduce significant inaccuracy to the estimated DEM error. This is actually one of the inherent weaknesses of SBAS technique that we noticed and has recently been pointed out by Fattahi and Amelung (2013). In short, both the single-master and multiple-master strategies possess their own advantages and disadvantages; however, we prefer multiple-master strategy, especially in the cases where the decorrelation is serious and the deformation is rapid. Once the interferogram stack has been generated, the HPQ points should be identified. In this section, we will introduce several methods that are widely used in current MTInSAR techniques with an emphasis on their weaknesses.

3.1. Interferogram stack

The observations of MTInSAR techniques are interferograms generated from a set of co-registered radar images. To co-register the images acquired over the area of interest on different dates with slightly different looking positions, one image should be selected as a reference that is also known as a master image. One general requirement on the selection of master image is to maximise the total coherence of the stacked interferograms. To this end, the decorrelation due to

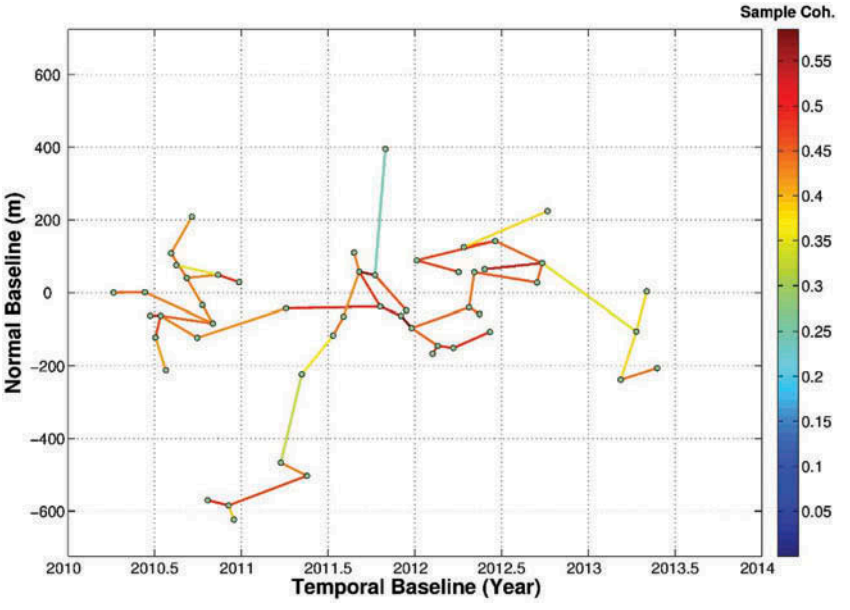

Figure 4. The MST graph constructed according to the mean coherence of sampled pixels in each interferogram. Only the interferograms than can maximise the total coherence are included in the tree graph.

the spatial–temporal baselines and Doppler frequency difference need to be considered and the total coherence (ρ_{total}) can be modelled by (Hooper *et al.* 2007)

$$\rho_{\text{total}} \approx \left(1 - f\left(\frac{T}{T^{\text{c}}}\right)\right) \cdot \left(1 - f\left(\frac{B_{\perp}}{B_{\perp}^{\text{C}}}\right)\right) \cdot \left(1 - f\left(\frac{F_{\text{DC}}}{F_{\text{DC}}^{\text{C}}}\right)\right) \tag{2}$$

where $f(x) = \begin{cases} x, \text{for } x \leq 1 \\ 1, \text{for } x > 1 \end{cases}$, superscript c denotes the critical values which should be determined according to the SAR dataset. It is worth noting that the reliability of the Equation (2) can be affected by ground features. For instant, the coherence of a vegetated area is much worse in summer than that with the same time span in winter. It means the temporal baseline itself sometimes cannot well reflect the quality of interferograms. Therefore, one more reasonable method is to calculate the coherence of all interferograms first and select either single-master stacked or multiple-master stacked interferograms according to the calculated coherence. Instead of calculating the coherence of all pixels, a very small portion of pixels sampled, say, by intensity variation can be used to reduce the computation burden. For the multiple-master stack, we can use the minimum spanning tree (MST) to select interferograms that can maximise the total coherence (Refice *et al.* 2006, Wang *et al.* 2012). As an example, Figure 4 shows the MST generated from a stack of TerraSAR-X interferograms over Hong Kong according to the sampled coherence.

3.2. HPQ points

As mentioned before, the HPQ points are the pixels having low decorrelation. There are basically two types of HPQ points. One type consists of points that can keep HPQ in interferograms with any baselines. In other words the backscatterer features of these points are little affected by the spatial–temporal decorrelation. These points are the main observations of the first generation of MTInSAR techniques and denoted with different names, for example persistent scatterers, permanent scatterers, PS (Ferretti *et al*. 2001, Hooper *et al*. 2004). Since these points might be involved in interferograms with extremely long baselines, the conventional coherence map that is widely used for assessment of interferogram quality is not adequate to identify these points. Instead, the analysis of intensity variance (Ferretti *et al*. 2001) or spatial correlation of phases (Hooper *et al*. 2004) is proven to be effective. Physical objects that can be classified into this type are abundant no matter in urban areas (e.g. buildings and lamp-posts) or in nonurban areas (e.g. rocks, and even dry mud). The other type is composed of points that can only keep high coherence in interferograms with baselines less than a certain length. The phase noise at these points is getting serious as the baseline increases. These points occupy a large portion of observations in multiple-master MTInSAR techniques (e.g. SBAS, CPT and TCPInSAR). However, the density of these points heavily depends on the baseline criteria which are mainly determined according to the operator's experience. The coherence map can well serve as a selector to isolate these points.

3.3. HPQ point identification methods

3.3.1. Amplitude dispersion index

The amplitude dispersion index (ADI) was first introduced by Ferretti and others (2000, 2001) in their PSInSAR technique, which employs a stack of single-master interferograms without considering baseline limitations. According to simulation tests the ADI is a satisfactory approximation for phase dispersion of pixels with high signal-to-noise ratio (SNR) and is defined as the ratio between the standard deviation (σ_A) and the mean (m_A) of multi-temporal backscattering intensity variations (Ferretti *et al*. 2000):

$$D_A = \frac{\sigma_A}{m_A} \tag{3}$$

Figure 5(b) shows an ADI map calculated from a stack of 19 TerraSAR-X SLC images over west Kowloon of Hong Kong. HPQ points selected with a D_A threshold of 0.25 are shown in Figure 5(c). The bright scatterers corresponding to the cargo containers were not selected as HPQ points due to the temporal variations of their backscattered intensities, which is in line with our expectations. Although several points in the sea were mistakenly selected, the performance of ADI is satisfactory. The main limitation is that the criteria is too tight to select densely enough points over nonurban settings.

3.3.2. Phase stability

In order to identify a sufficient number of coherent points especially in nonurban areas where scatterers usually have low SNR, Hooper and others (2004) proposed a HPQ point selection method based on the phase stability of targets. Phase stability is analysed under the assumption that deformation is spatially correlated. The phase values of neighbouring

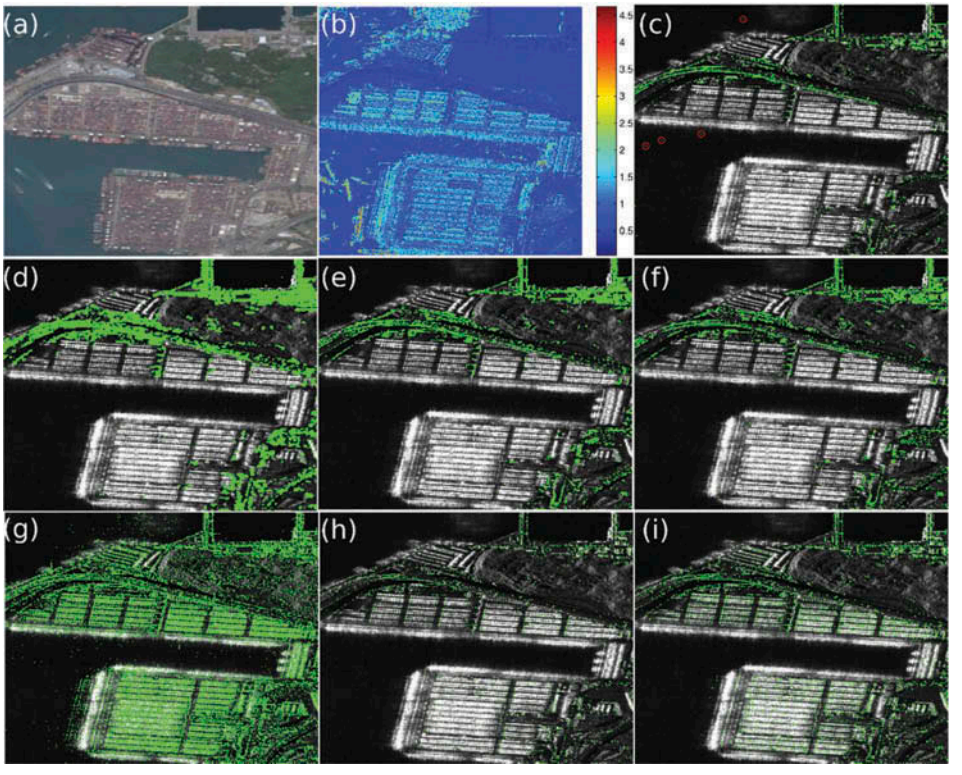

Figure 5. Examples of HPQ point selection by different methods: (a) optical image of the testing area; (b) ADI map; (c) selected HPQ points by ADI with a threshold of 0.25 where points in the sea as circled were mistakenly selected; (d) HPQ points selected by conventional coherence map with a threshold of 0.25; (e) HPQ points selected by improved coherence map with a threshold of 0.25; (f) HPQ points selected according to phase stability; (g, h) HPQ points selected by SCR method using thresholds of 0.1 and 0.2, respectively; (i) HPQ points selected by spectral diversity (threshold: 1.2).

PS candidates are averaged, and those with lowest residual noise (variability) are selected. Given a set of topographically corrected interferograms, a measure of phase stability can be defined as (Hooper *et al*. 2004)

$$\gamma_x = \frac{1}{N}\left|\sum \exp\{\, j(\Phi_{\text{int},x,i} - \bar{\Phi}_{\text{int},x,i} - \Delta\hat{\Phi}_{\varepsilon,x,i})\}\right| \tag{4}$$

where N is the number of interferograms, $\Phi_{\text{int},x,i}$ is the differential phase of the xth interferogram, $\bar{\Phi}_{\text{int},x,i}$ is the mean phase of all PS candidates within a circular patch centred on pixel x with radius L and $\Delta\hat{\Phi}_{\varepsilon,x,i}$ is the estimated phase component contributed by DEM errors. To calculate the mean phase of patches efficiently, PS candidates selected using the ADI method with a high threshold value are taken as initial selections. The threshold value of γ_x is selected in a probabilistic fashion. Figure 5(f) presents the location of HPQ points selected according to phase stability using the same TerraSAR-X datasets. The density of points is notably higher than that by ADI.

3.3.3. Coherence map

The coherence map method has long been used to select HPQ points from interferograms with relatively short baselines. After eliminating the phase components related to topography and flat Earth, the coherence value of each pixel in selected interferograms can be estimated. Recent years have seen the rapid development of advanced coherence estimation methods (e.g. Zebker and Chen 2005, Jiang *et al*. 2015) which can reduce the bias without much loss of resolution. After the coherence estimation for each pixel in all selected interferograms, the pixels with minimum coherence value larger than a threshold are identified as HPQ points. As an example, Figure 5(d) and (e) present selected HPQ points using conventional and advanced coherence estimation methods (Jiang *et al*. 2015), respectively. It is clear Figure 5 (d) appears to be not as sharp as that by the improved method (Figure 5(e)). Compared with ADI method, the coherence map usually can select several times more points.

3.3.4. Signal-to-clutter ratio

The signal-to-clutter ratio (SCR) approach was first suggested by Adam to select point targets for their PSI processor. With an assumption that a PS observation consists of a deterministic signal that is disturbed by random circular Gaussian distributed clutter, the SCR can be estimated by computing the ratio of the power of a PS candidate over that of its immediate neighbouring pixels. The relationship between the SCR and the phase standard variance (σ_ϕ) can be defined as (Freeman 1992, Adam 2004)

$$\sigma_\phi = \frac{1}{\sqrt{2 \cdot \mathrm{SCR}}}, \mathrm{SCR} = \frac{s^2}{c^2} \tag{5}$$

where s represents the amplitude of the dominant scatterer and c the clutter in the surroundings. Equation (5) can be used to determine a reasonable threshold of SCR. For example, if a phase standard variance of 0.5 rad^2 is desired, the minimum of SCR value is 2. Since the SCR estimation can be performed with a single image, the SCR method has less requirement on the size of datasets compared with ADI. As an example, Figure 5(g) and (h) show the selected HPQ points by SCR method using the thresholds of 0.1 and 0.2, respectively.

3.3.5. Spectral diversity

According to the fact that the spectral behaviour of well-focused dominating point targets is different with that of distributed targets, HPQ points can also be selected. The physical basis for this method is that for point targets almost the same backscattering intensity is found when processing different looks with fractional azimuth and range bandwidth (Werner *et al*. 2003). Advantages of this method are that it works for the cases where only a small number of images are available and it has less requirement on radiometric calibration. Figure 5(i) shows the selected HPQ points according to spectral diversity using a threshold of 1.2.

Besides the aforementioned methods, there are several other methods that have been developed and used in MTInSAR processing routines, for example maximum likelihood estimation (Shanker and Zebker 2007) and DespecKS (Ferretti *et al*. 2011). More recently, methods that can identify or predict HPQ points according to land cover maps have also been proposed (e.g. Cigna *et al*. 2014).

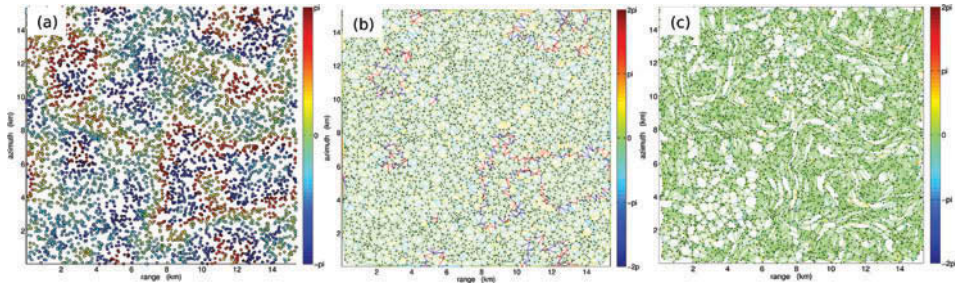

Figure 6. (a) Simulated atmospheric artefacts at coherent points; (b) atmospheric artefacts at arcs constructed by Delaunay triangulation; (c) atmospheric artefacts at arcs constructed by gradient-based networking.

3.4. *Points VS arcs*

Due to the existence of phase ambiguities, phase measurements at a single HPQ point are meaningless and cannot be directly used for the retrieval of parameters of interest. There are two strategies to deal with the wrapped phases. One is unwrapping the HPQ points in each interferogram. Once the ambiguity integers have been eliminated, phases at HPQ points would reflect obvious contributions of deformation, DEM error, orbit inaccuracy, atmospheric artefacts and other noise, and can be employed as observations of MTInSAR techniques (e.g. SBAS). On the other hand, phase differences at arcs construed among neighbouring HPQ points can also be taken as observations. Actually this strategy has been adopted by most MTInSAR techniques. Technical innovations lie in how to deal with the integer ambiguities in phase differences. For instance, ambiguities can be estimated or eliminated by 3D phase unwrapping (e.g. StaMPS), integer least squares (e.g. STUN) and maximum ensemble coherence (e.g. PSInSAR, CPT). Arcs having ambiguities can also be detected and removed by an outlier detector (e.g. TCPInSAR). One advantage of taking arcs as observations which has long been addressed is that spatial correlated atmospheric artefacts can be largely reduced. This is generally true for most arcs, although there are unavoidably some arcs at which the atmospheric components have been enlarged. Figure 6 shows simulated atmospheric phases at HPQ points and arcs. Arcs in Figure 6(b) and (c) are constructed by Delaunay and phase gradient–aided method, respectively. It is clear that in Figure 6(b) there are some arcs having larger phase values than at points. When the phase spatial variations are considered (i.e. Figure 6(c)), the number of those arcs can be significantly reduced.

4. Modelling

The phase values at HPQ points, which are related to several parameters we are seeking (Equation (1)), are the basis of MTInAR modelling. Considering M interferograms generated from N SLC images and G arcs constructed from P HPQ points according to an index matrix C where the column corresponding to the point with known DEM error and deformation has been removed. For a given pixel x, it has a perpendicular baseline vector $B_{\perp,x} = -(4\pi/\lambda)\cdot(1/\rho\sin\theta)\left[B^1_{\perp,x} \quad \cdots \quad B^i_{\perp,x} \quad \cdots \quad B^M_{\perp,x}\right]$ and a temporal baseline vector $B_t = -(4\pi/\lambda)\left[B^1_t \quad \cdots \quad B^i_t \quad \cdots \quad B^M_t\right]$. In this section, we will introduce the relationship between phase observations (either wrapped or unwrapped) and parameters.

4.1. Model for topographic error elimination

Recalling Equation (1), for a pixel x having an unwrapped topography-related phase observation in the ith differential interferogram ($\phi^i_{\text{dint},x}$), the contribution of topographic error can be modelled as

$$\phi^i_{\text{dint},x,\text{topo}} = -\frac{4\pi}{\lambda}\frac{\mathrm{B}^i_{\perp,x} h_{\text{res},x}}{R_x \sin\theta_x} \tag{6}$$

Considering a stack of observations in M interferograms, the function model can be expressed as

$$\phi_{\text{dint},x,\text{topo}} = B_{\perp,x} h_{\text{res},x} \tag{7}$$

where $\phi_{\text{dint},x,\text{topo}}$ is the observation vector contributed by topographic error, that is $\left[\phi^1_{\text{dint},x,\text{topo}} \quad \cdots \quad \phi^i_{\text{dint},x,\text{topo}} \quad \cdots \quad \phi^M_{\text{dint},x,\text{topo}}\right]^T$.

However, as stated in Section 3, if the phases at HPQ points are wrapped, we have to use phase difference at arcs as observations. In this case, for a given arc (g) that is constructed by point x and one of its neighbouring point. The relationship between the phase difference ($\Delta\phi^i_{\text{dint},g,\text{topo}}$) and the relative topographic error ($\Delta h_{\text{res},g}$) at the arc has an expression as

$$\Delta\phi^i_{\text{dint},g,\text{topo}} = -\frac{4\pi}{\lambda}\frac{\mathrm{B}^i_{\perp,x} \Delta h_{\text{res},g}}{R_x \sin\theta_x} \tag{8}$$

Similarly, we can get the vector form, as

$$\Delta\phi_{\text{dint},x,\text{topo}} = B_{\perp,x} \Delta h_{\text{res},x} \tag{9}$$

If the observation is dominated by the phase component related to topographic error, Equation (7) or Equation (9) can be used for topographic error estimation. Among current MTInSAR techniques, only StaMPS estimates the height-error-related component separately, while the direct parameter is not the height error but the so-called look angle error which is caused by the height error and the difference between the phase centre and the physical centre of the target (Hooper *et al*. 2004).

4.2. Model for deformation estimation

SAR image pairs with different time span reflect the temporal evolution of deformation and therefore can be used to retrieve the deformation time series. However, current MTInSAR techniques seldom estimate the deformation time series directly. Instead, the direct parameters employed by MTInSAR techniques are the linear deformation rate or velocity vector. By doing this, the stability and reliability of solution can be improved. For a given point (x), let $\bar{v}_x$ be the linear deformation rate and v_x be the deformation velocity vector including both linear and non-linear parts. Their relationships with the corresponding phase component vector are expressed as (Berardino *et al*. 2002)

$$\begin{aligned}\phi_{\text{dint},x,\text{lindefo}} &= B_{t,\text{sum}}\bar{v}_x \\ \phi_{\text{dint},x,\text{defo}} &= B_t v_x\end{aligned} \tag{10}$$

Similarly, for a given arc (g), the vector of phase differences at the arc has a relationship with the relative deformation rate and deformation rate vector as (Zhang *et al*. 2011)

$$\begin{aligned}\Delta\phi_{\text{dint},g,\text{lindefo}} &= B_t\Delta\bar{v}_g \\ \Delta\phi_{\text{dint},g,\text{defo}} &= B_t\Delta v_g\end{aligned} \tag{11}$$

4.3. *Model for orbit error estimation*

Orbit error in an interferogram can be modelled by a low-order polynomial. Since an interferogram is a linear combination of two SLC images, the orbit error can also be mathematically represented by a combination of two polynomials associated with SLC images. It should be noted that such polynomials do not have any physical meaning while by doing this the number of parameters to be estimated can be significantly reduced. Further assuming one reference image that is immune to the orbit error, the relative orbit error of a pixel x with coordinates (X,Y) with respect to the reference image is expressed as

$$\Delta\phi^j_{orb,slc,x} = a^j X + b^j Y + c^j XY,\ j = 1,\cdots,N-1 \tag{12}$$

where a^j, b^j and c^j are the unknown coefficients. The defined polynomials can be combined to describe the orbit phase in any interferogram. In the following, we only consider the case of observations consisting of wrapped phases. The relative orbit errors at all arcs in an SLC image can be written as

$$\Delta\phi^j_{\text{orb,slc}} = a^j dX + b^j dY + c^j dXY,\ j = 1,\ldots,N-1 \tag{13}$$

where dX, dY and dXY are the vectors of pixel coordinate differences. The matrix form of Equation (12) is

$$\Delta\phi^j_{\text{orb,slc}} = D^j P^j_{\text{slc,orb}},\ j = 1,\ldots,N-1 \tag{14}$$

where $D^j = [\,dX \quad dY \quad dXY\,]$ and $P^j_{\text{slc,orb}} = [\,a_j \quad b_j \quad c_j\,]^T$. Let A be a matrix for interferometric operation to generate M interferograms from N SLC images (Zhang *et al*. 2014). The design matrix linking the observations at arcs and orbit error parameters is

$$D_{\text{orb}} = A \otimes D \tag{15}$$

where $\otimes$ denotes the Kronecker tensor product. The phase components due to orbit errors at all arcs of interferograms can then be defined as

$$\Delta\phi_{\text{orb}} = D_{\text{orb}} P_{\text{orb}} \tag{16}$$

We refer readers who are interested in the details of orbit error modelling to Zhang *et al*. (2014).

4.4. Typical MTInSAR models

4.4.1. Point-based model

For the unwrapped phase observations, the contribution of DEM error and linear deformation is expressed as

$$\phi_{\text{dint},x,\text{topo}} + \phi_{\text{dint},x,\text{lindefo}} = \begin{bmatrix} B_{\perp,x} & B_{t,\text{sum}} \end{bmatrix} \begin{bmatrix} h_{\text{res},x} \\ \bar{v}_x \end{bmatrix} \tag{17}$$

Provided that the remained terms have a relatively small magnitude and can be safely taken as noise, the observation model for estimation of DEM error and linear deformation rate has the following form:

$$\phi_{\text{dint},x} = \begin{bmatrix} B_{\perp,x} & B_{t,\text{sum}} \end{bmatrix} \begin{bmatrix} h_{\text{res},x} \\ \bar{v}_x \end{bmatrix} + \phi_{\text{noise}} \tag{18}$$

After eliminating the phase contribution of DEM error, the remained phase is mainly contributed by deformation which can be modelled as

$$\phi_{\text{dint},x,\text{defo}} = B_t v_x \tag{19}$$

Although most current MTInSAR techniques employ two steps to separate DEM error and deformation signal, there is also a promising model proposed by Samsonov *et al*. (2011) that can jointly estimate the DEM error and successive deformation rate vector from a set of unwrapped short baseline interferograms. The model can be expressed as (Samsonov *et al*. 2011)

$$\phi_{\text{dint},x} = \begin{bmatrix} B_{\perp,x} & B_{t,\text{sum}} \end{bmatrix} \begin{bmatrix} h_{\text{res},x} \\ v_x \end{bmatrix} + \phi_{\text{noise}} \tag{20}$$

Since the number of unknowns in the model is larger than the effective observations whose number is one less than the amount of SLC images, least squares, as the solver, is enhanced by minimum-norm criteria that is implemented via singular value decomposition (SVD).

4.4.2. Arc-based model

Arc-based MTInSAR model can be derived similarly as point-based model. We give here directly the equation for estimation of relative topography error and deformation rate at arcs (Zhang *et al*. 2011).

$$\Delta\phi_{\text{dint},g} = \begin{bmatrix} B_{\perp,x} & B_{t,\text{sum}} \end{bmatrix} \begin{bmatrix} \Delta h_{\text{res},g} \\ \Delta\bar{v}_g \end{bmatrix} + \Delta\phi_{\text{noise},g} \tag{21}$$

Orbit error can also be jointly modelled together with topographic error and deformation rate (Zhang *et al*. 2014). The joint model has the form as

$$\underset{(M\times G)\times 1}{\Delta\phi_{\text{all,arcs}}} = DP + \underset{(M\times G)\times 1}{W} \tag{22}$$

with

$$\begin{aligned} D &= [\,D_{\text{par}} \quad D_{\text{orb}}\,] \\ P &= [\,P_{\text{par}} \quad P_{\text{orb}}\,] \end{aligned} \tag{23}$$

where D_{par} is the design matrix relating the observations and deformation rate and topographic error at each coherent point except for one reference point, that is P_{par}.

5. Parameter estimation

The advances in MTInSAR techniques have been driven by not only the availability of abundant SAR data but also the evolving parameter estimation methods. The bulk of studies of MTInSAR technique actually lie in how to retrieve deformation parameters from the wrapped phases at these high-quality points selected. The integer ambiguities associated with the phase measurements hinder a direct estimation, therefore one natural solution is unwrapping each interferogram first to eliminate the ambiguities, which is a routine processing of SBAS. This solution is preferred by SBAS simply because successful unwrapping at selected points is only possible for interferograms with relatively short baselines. However, in some extreme cases the success rate cannot be guaranteed, which motivated the development of robust parameter estimation methods (e.g. Lauknes *et al.* 2011) that can well suppress the effects of wrongly unwrapped phases at the cost of low computing efficiency. When solving deformation time series from these phases without phase ambiguities (see Equation (18)), it is possible that the number of observations is not enough for parameter estimation. In other words, the design matrix is rank deficient, which means there are an infinite number of solutions. To tackle this problem, SVD has been proposed and used by SBAS (Beradino *et al.*, 2002). The reason why SVD could result in a reasonable solution in many cases is that by SVD a minimum-norm constraint has been added to the parameters besides the least squares criterion. This constraint is reasonable when taking velocities at each temporal intervals rather than deformations as parameters, an inherent requirement of SBAS. Besides directly unwrapping the observations, there are several methods that estimate the parameters directly from wrapped phases. Among them the most widely used one is denoted as temporal coherence maximisation (Ferretti *et al.* 2001, Colesanti *et al.* 2003, Mora *et al.* 2003). As a non-linear inversion problem, the method conducts a search through the solution space to maximise a temporal coherence index and therefore determine the parameters, typically the DEM errors and the predefined deformation model (e.g. linear rate). 3D unwrapping implemented in StamMPS is also an excellent method. Integer phase ambiguities can also be taken as parameters together with those of our interests as proposed by Kampes and Hanssen (2004). Integer least squares is then used to resolve the solution. In addition, linear inversion is also possible for parameter estimation directly from wrapped phases provided that the observations having phase ambiguities can be well detected and removed. This is the theoretical basis of methods proposed by Zhang *et al.* (2011, 2012). In the following, we will give a brief introduction on these estimation methods.

5.1. Linear inversion with unwrapped observations

When the observations are the unwrapped phases, the parameters can be retrieved by a least squares approach from Equation (18).

$$\begin{bmatrix} \hat{h}_{\mathrm{res},x} \\ \hat{\bar{v}}_x \end{bmatrix} = (B_x{}^{\mathbf{T}} B_x)^{-1} B_x{}^{\mathbf{T}} \phi_{\mathrm{dint},x} \tag{24}$$

where $B_x = \begin{bmatrix} B_{\perp,x} & B_{t,\mathrm{sum}} \end{bmatrix}$. It should be noted that although there are two resolved parameters, in SBAS only the DEM error term (h) is used for eliminating the phase component caused by topographic residuals. A re-unwrapping operation at the HPQ points is closely followed to reduce the unwrapping errors caused by topographic residuals. From the re-unwrapped phases where the deformation-related signal is dominated, the deformation rates at successive temporal intervals can be resolved by minimum-norm least squares, which in SBAS technique are implemented by SVD.

5.2. Linear inversion with wrapped observations

5.2.1. Integer least squares

When the observations are the wrapped phase differences at arcs and the parameters are velocity difference (Δv_g), height error difference (Δh_g) and integer ambiguities (N) in a total of M interferograms, Equation (21), can be rewritten as (Kampes 2006)

$$\Delta\phi_{\mathrm{dint},g} = \begin{bmatrix} -2\pi & & & \\ & -2\pi & & \\ & & \ddots & \\ & & & -2\pi \end{bmatrix} \begin{bmatrix} N^1 \\ N^2 \\ \vdots \\ N^M \end{bmatrix} + B_g \begin{bmatrix} \Delta h_{\mathrm{res},g} \\ \Delta\bar{v}_g \end{bmatrix} + \Delta\phi_{\mathrm{noise}} \tag{25}$$

For each arc, M integer ambiguities and two real-valued parameters have to be estimated from M observed wrapped phase differences. The solution to this system can only be obtained by using *a priori* knowledge of the integer nature of the ambiguities (Kampes and Hanssen 2004). Integer least squares method is used by STUN for parameter estimation.

5.2.2. Least squares with ambiguity detector

For an MTInSAR system in which multi-master interferograms with short baselines (spatial and temporal) are involved, there are usually sufficient arcs constructed by neighbouring coherent pixels that do not have phase ambiguities. If these arcs can be reliably identified, parameter estimation on these arcs can be greatly simplified. For any arc regardless of phase ambiguities, the least squares solution of unknowns from Equation (21) is as follows:

$$\begin{aligned} \begin{bmatrix} \Delta h_{\mathrm{res},g} \\ \Delta v_g \end{bmatrix} &= (B_g{}^{\mathbf{T}} \mathbf{P}_g B_g)^{-1} (B_g{}^{\mathbf{T}} \mathbf{P}_g \Delta\phi_{\mathrm{dint},g}) \\ R &= \Delta\phi_{\mathrm{dint},g} - (B_g{}^{\mathbf{T}} \mathbf{P}_g B_g)^{-1} (B_g{}^{\mathbf{T}} \mathbf{P}_g \Delta\phi_{\mathrm{dint},g}) \end{aligned} \tag{26}$$

where R is the least squares residual vector and $P_g$is the weight matrix, which can be obtained by taking the inverse of a prior variance matrix of the double-difference phases (Zhang *et al*. 2011). Experience shows that the least squares residuals for an arc with and without phase ambiguities are quite different, indicating that phase ambiguities can bias the parameter estimation significantly (Zhang *et al*. 2011, 2012). Therefore, an ambiguity detector can be designed by taking account of the least squares residuals. After removing the arcs with phase ambiguities, parameters for the remaining arcs are integrated to obtain parameter estimates at all coherent points with respect to a designated reference point.

5.3. *Non-linear inversion with wrapped observations*

Since observation vector is ambiguous, the parameter estimation from Equation (19) is a non-linear inversion problem. A temporal coherence index (γ_g) is commonly used for this inversion (Ferretti *et al*. 2001, Mora *et al*. 2003). Given a total of M interferograms, $\gamma_g$is defined as

$$\gamma_g = \frac{1}{M}\left|\sum_{i=1}^{M} e^{-j\Delta\phi^i_{\text{noise},g}}\right| \tag{27}$$

where $j=\sqrt{-1}$. By setting appropriate variation ranges for the velocity difference (Δv_g) and height error difference ($\Delta h_{\text{res},g}$), one can search for the maximum coherence, γ_g, within the specified two-dimensional ranges using small sampling intervals. Then the values for Δv_g and $\Delta h_{\text{res},g}$can be found. When Δv_g and $\Delta h_{\text{res},g}$ for all neighbouring pixel sets are determined, the absolute values of DEM error and linear deformation rate at each coherent pixel can be derived through spatial integration with respect to an arbitrary reference point, where the DEM error and linear deformation rate are known or assumed to be zero. Note that the solution search can only be successfully performed under the condition of $\left|\omega^k_{i,x,y}\right|<\pi$, which can be met in most cases. The method is applicable to both single-master and multiple-master InSAR stacks. However, the limitation associated with this method is that the solution searched cannot be guaranteed to be unique. In other words, there are several solutions corresponding to the same peak at some arcs. As an example, Figure 7 shows the coherence map at the solution searching procedure at one arc where more than one solution pairs can reach the peak of ensemble coherence.

5.4. *3D phase unwrapping*

There is another popular way to retrieve the deformation parameters, termed 3D phase unwrapping (Hooper 2006), which is implemented in StaMPS. It is based on the fact that phase differences at arcs usually appear to have small spatial variations (typically less than half a cycle) while having large temporal variations. In 3D wrapping, the phase differences at arcs are first unwrapped in temporal domain under the assumption that the deformation signal is smooth. The unwrapped results are used to build a probability density function for the phase differences at arcs in each interferogram and then the optimisation routines of statistical-cost, network-flow algorithm for phase unwrapping (SNAPHU) (Chen 2001) are applied to search for the most likely positions of phase ambiguities. The cost function is derived not only by SNAPHU itself but also by some additional requirements such as that phase jumps cannot be placed between grid cells

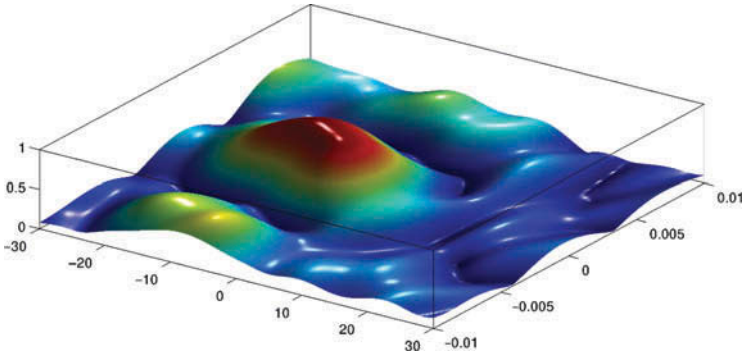

Figure 7. An example of solution space searching used by PSI where multiple parameters correspond to the same peak of ensemble coherence, indicating that unique solution cannot be guaranteed.

interpolated from the same sparse value and that the probability of phase jumps between other cells depends on the evolution of the phase difference between the cells with time (Sousa *et al*. 2011).

As a summary, Table 1 shows the estimators used by several current MTInSAR techniques where the observation type as well as the methods for coherent point selection are also addressed.

5.5. Deformation estimation over Zhanghua-Yunlin area in Taiwan

We conduct a comparative study over four parameter estimators (i.e. linear inversion with ambiguity detector used in TCPInSAR, 3D unwrapping used in StaMPS and least squares used in SBAS and Samsonov's method) aiming to validate their performance. A total of 14 Envisat/ASAR images acquired from January 2007 to September 2008 over Zhanghua-Yunlin area (Figure 8) in Taiwan are used as testing data. The HPQ points are selected, respectively, using phase stability method and improved coherence map method. It is clear

Table 1. Comparison among parameter solvers used by current MTInSAR techniques.

Techniques	Interferogram type	Observation	Point selection	Parameter solver
PSInSAR/ PSI	Single master	Arc	ADI	Temporal coherence maximisation
SBAS	Multiple master	Point	Coherence	Minimum-norm least squares
StaMPS	Single/multiple master	Arc	Phase stability	3D unwrapping
CPT	Multiple master	Arc	ADI and coherence	Temporal coherence maximisation
STUN	Single master	Arc	ADI and SCR	Weighted integer least squares
Pi-rate	Multiple master	Point	Coherence	Least squares with Laplacian smoothing
IPTA	Single master	Arc	ADI and SD	Temporal coherence maximisation
Samsonov's	Multiple master	Point	Coherence	Minimum-norm least squares
TCPInSAR	Multiple master	Arc	Coherence	Least squares with ambiguity detector

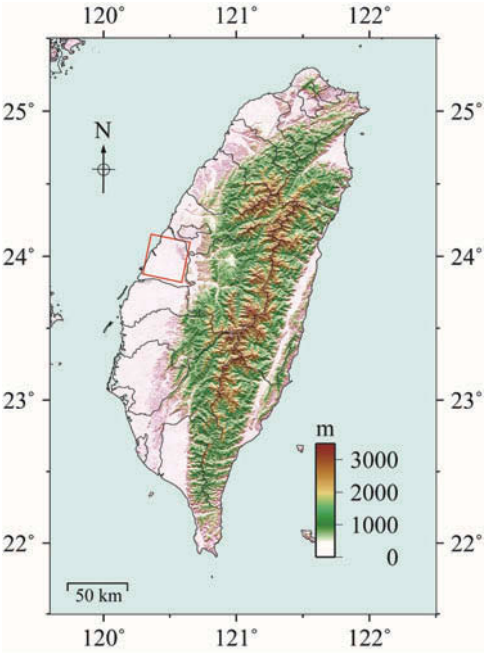

Figure 8. The location of the study area overlapped on SRTM DEM Map. The box outlines the studied area.

that both methods can select abundant HPQ points in the area of interest. Following the respective estimation procedure, the deformation signal has been retrieved and the deformation rates are shown in Figure 9. A comparison among InSAR-derived deformation time series at five GPS stations is shown in Figure 10. It is observed that the deformation patterns retrieved by these estimators are generally consistent, while there are areas having discrepancy. In our opinion, the discrepancy is mainly resulted by improper selection of parameters (e.g. window size of the filter and threshold) when implementing these estimators and cannot indicate one method has better performance than others.

6. Conclusion

The MTInSAR technique is gaining more and more popularity for deformation monitoring over the past decade. Compared with the original form, the MTInSAR technique itself has evolved significantly almost in every step of the processing chain. However, the ultimate goal of technique remains unchanged. How to accurately retrieve the signals of interests at highest resolution in a most efficient way is always the central concern of current MTInSAR technical branches. To this end, abundant advanced algorithms have been developed and some of them released as open-source software packages have achieved vast applications. The progress in MTInSAR techniques indeed provides a solid underpinning for its future development. There are several possible areas for further research including efforts aimed at:

(1) Providing optimal observations for MTInSAR technique. The starting point of all MTInSAR techniques is the co-registered SAR images. The co-registration

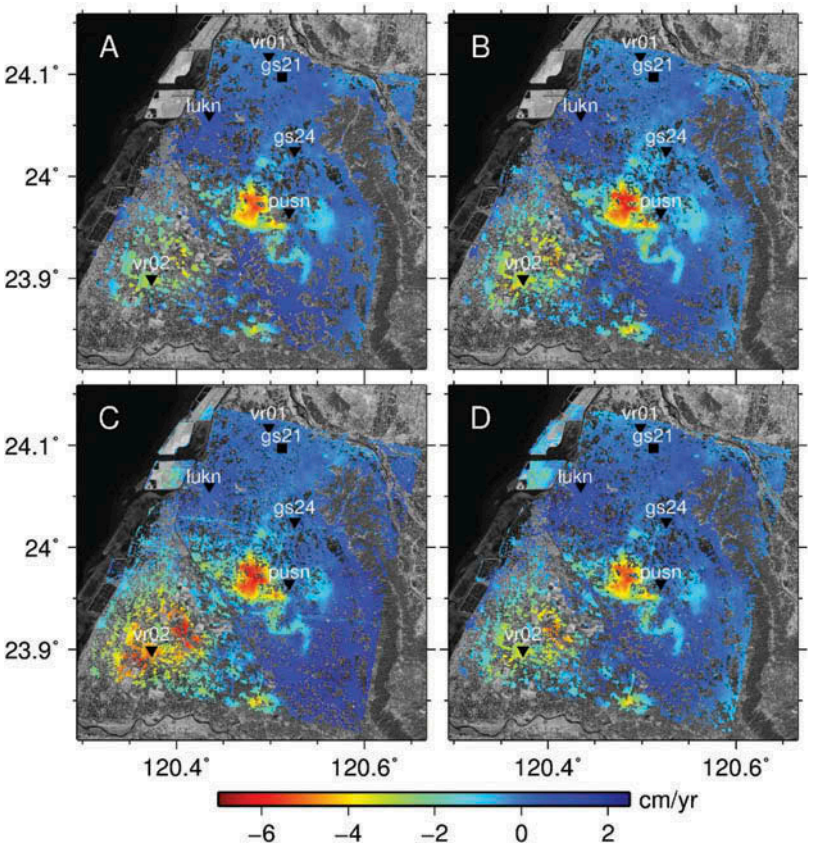

Figure 9. Comparison among deformation results retrieved by four MTInSAR methods: (a) SBAS; (b) Samsonov's SBAS; (c) StaMPS and (d) TCPInSAR. The black square (gs21) represents the reference point and the black triangles are the GPS stations for comparison of InSAR-derived deformation time series.

is designed for the whole image rather than the HPQ points, which could result in possible phase errors for HPQ points. A HPQ-based co-registration strategy should be developed to avoid such error. Many thresholds are used in current MTInSAR techniques for like, HPQ selection, interferogram selection and also for parameter estimation, while proper selection of these thresholds is sometimes very challenging and often largely depends operators' experience. It actually indicates current techniques should be further optimised. In addition, there is still room for improvement on network construction for arc-based MTInSAR techniques, so that the constructed arcs have proper density and can better suppress the effects of atmospheric artefacts.

(2) Advanced modelling. Joint estimation of several signals together can better utilise the spatial–temporal features of these signals and therefore better isolate the interested signals, which has been proved effective by, for example a joint model for simultaneous estimation of orbit error and deformation. However, there is no robust model for jointly estimating the DEM error and deformation time series. Such a model will be particularly helpful for multiple-master-based

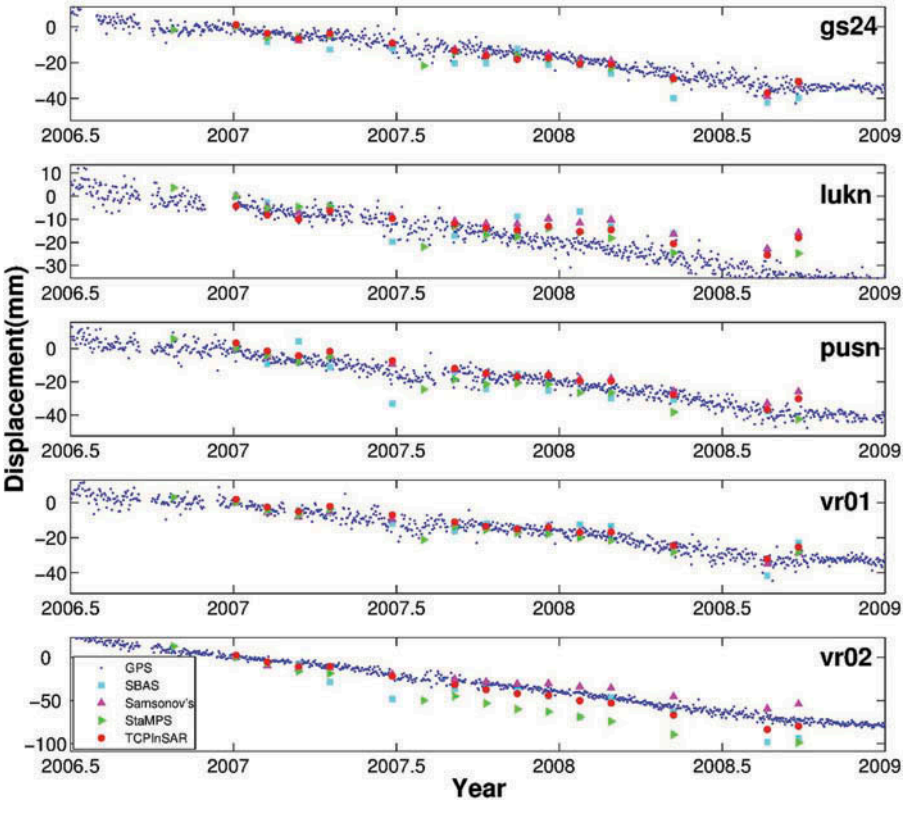

Figure 10. Deformation time series derived by the four MTInSAR methods at five GPS stations shown in Figure 9.

MTInSAR techniques where the topography error is often poorly estimated due to improper assumption of deformation evolution.

(3) Developing a universal parameter estimator. Although many parameter estimators are available in current MTInSAR techniques, it is quite often to see discrepancies existing among the results from these estimators. It partially reflects the limitations of these estimators. Actually there is a lack of a universal estimator. When designing an estimator, we should consider how well it can estimate the phase ambiguity or avoid the phase unwrapping error and how well it can suppress or even estimate the atmospheric artefacts. If the estimator can well meet the aforementioned requirements, its applicability is expected to be universal.

(4) Designing a proper quality assessment method. Quality assessment of InSAR-derived results is not an easy task. Obviously the comparison with other measurements (e.g. those from levelling and GPS) that are wildly used in publications owns many limitations and cannot be accepted as an effective method. Variance and covariance component estimation (VCE) from phase residuals can also not reliably tell the accuracy of the estimated parameters simply due to the existence of atmospheric artefacts. Proper quality assessment via VCE could be possible provided that the atmospheric artefacts can be well isolated.

Acknowledgements

The Envisat/ASAR data used in the study are copyrighted by European Space Agency.

Disclosure statement

No potential conflict of interest was reported by the authors.

Funding

The research is partly supported by the Research Grants Council of the Hong Kong Special Administrative Region [project number PolyU 5381/13E], [project number PolyU 152214/14E], [project number PolyU 152043/14E]; the National Natural Science Foundation of China [grant number 41304011], [grant number 41374013], [grant number 41222027]; public welfare project of National Administration of Surveying, Mapping and Geoinformation of China.

References

Adam, N., 2004. *Development of a scientific permanent scatterer system: modifications for mixed ERS/ENVISAT time series*. ENVISAT and ERS Symposium, Salzburg, Austria, 6–10 September, 2004, pp. 1–9.

Adam, N., *et al*., 2009. Practical persistent scatterer processing validation in the course of the Terrafirma project. *Journal of Applied Geophysics*, 69 (1), 59–65. doi:10.1016/j.jappgeo.2009.07.002

Berardino, P., *et al*., 2002. A new algorithm for surface deformation monitoring based on small baseline differential SAR interferograms. *IEEE Transactions on Geoscience and Remote Sensing*, 40 (11), 2375–2383. doi:10.1109/TGRS.2002.803792

Biggs, J., *et al*., 2007. Multi-interferogram method for measuring interseismic deformation: Denali Fault, Alaska. *Geophysical Journal International*, 170 (3), 1165–1179. doi:10.1111/gji.2007.170.issue-3

Casu, F., Manzo, M., and Lanari, R., 2006. A quantitative assessment of the SBAS algorithm performance for surface deformation retrieval from DInSAR data. *Remote Sensing of Environment*, 102 (3–4), 195–210. doi:10.1016/j.rse.2006.01.023

Chang, L. and Hanssen, R.F., 2014. Detection of cavity migration and sinkhole risk using radar interferometric time series. *Remote Sensing of Environment*, 147, 56–64. doi:10.1016/j.rse.2014.03.002

Chen, C.W., 2001. *Statistical-cost network-flow approaches to two-dimensional phaseunwrapping for radar interferometry*. Thesis (PhD). Stanford University.

Cigna, F., *et al*., 2014. Simulating SAR geometric distortions and predicting persistent scatterer densities for ERS-1/2 and ENVISAT C-band SAR and InSAR applications: nationwide feasibility assessment to monitor the landmass of Great Britain with SAR imagery. *Remote Sensing of Environment*, 152, 441–466. doi:10.1016/j.rse.2014.06.025

Colesanti, C., *et al*., 2003. Monitoring landslides and tectonic motions with the permanent scatterers technique. *Engineering Geology*, 68 (1–2), 3–14. doi:10.1016/S0013-7952(02)00195-3

Crosetto, M., *et al*., 2010. Persistent scatterer interferometry. *Photogrammetric Engineering & Remote Sensing*, 76 (9), 1061–1069. doi:10.14358/PERS.76.9.1061

Ding, X.-L., *et al*., 2008. Atmospheric effects on InSAR measurements and their mitigation. *Sensors*, 8 (9), 5426–5448. doi:10.3390/s8095426

Fattahi, H. and Amelung, F., 2013. DEM error correction in InSAR time series. *Geoscience and Remote Sensing, IEEE Transactions on*, 51 (7), 4249–4259. doi:10.1109/TGRS.2012.2227761

Feng, G., *et al*., 2010. Coseismic fault slip of the 2008 Mw 7.9 Wenchuan earthquake estimated from InSAR and GPS measurements. *Geophysical Research Letters*, 37, 1. doi:10.1029/2009GL041213

Ferretti, A., *et al*., 2011. A new algorithm for processing interferometric data-stacks: SqueeSAR. *IEEE Transactions on Geoscience and Remote Sensing*, 49 (9), 3460–3470. doi:10.1109/TGRS.2011.2124465

Ferretti, A., Prati, C., and Rocca, F., 2000. Nonlinear subsidence rate estimation using permanent scatterers in differential SAR interferometry. *IEEE Transactions on Geoscience and Remote Sensing*, 38 (5), 2202–2212. doi:10.1109/36.868878

Ferretti, A., Prati, C., and Rocca, F., 2001. Permanent scatterers in SAR interferometry. *IEEE Transactions on Geoscience and Remote Sensing*, 39 (1), 8–20. doi:10.1109/36.898661

Freeman, A., 1992. SAR calibration: an overview. *IEEE Transactions on Geoscience and Remote Sensing*, 30 (6), 1107–1121. doi:10.1109/36.193786

Fruneau, B. and Sarti, F., 2000. Detection of ground subsidence in the city of Paris using radar interferometry: isolation of deformation from atmospheric artifacts using correlation. *Geophysical Research Letters*, 27 (24), 3981–3984. doi:10.1029/2000GL008489

Gabriel, A.K., Goldstein, R.M., and Zebker, H.A., 1989. Mapping small elevation changes over large areas: differential radar interferometry. *Journal of Geophysical Research: Solid Earth (1978–2012)*, 94 (B7), 9183–9191.

Gong, W., *et al*., 2015. Temporal filtering of InSAR data using statistical parameters from NWP models. *IEEE Transactions on Geoscience and Remote Sensing*, 53 (7), 4033–4044. doi:10.1109/TGRS.2015.2389143

Hanssen, R.F., 2001. *Radar interferometry: data interpretation and error analysis*. Dordrecht: Kluwer Academic Publishers.

Hilley, G.E., *et al*., 2004. Dynamics of slow-moving landslides from permanent scatterer analysis. *Science*, 304 (5679), 1952–1955. doi:10.1126/science.1098821

Hooper, A., 2006. *Persistent scaterrer radar interferometry for crustal deformation studies and modeling of volcanic deformation*. Thesis (PhD). Stanford University.

Hooper, A., Segall, P., and Zebker, H., 2007. Persistent scatterer interferometric synthetic aperture radar for crustal deformation analysis, with application to Volcán Alcedo, Galápagos. *Journal of Geophysical Research: Solid Earth*, 112 (B07407). doi:10.1029/2006JB004763

Hooper, A., *et al*., 2004. A new method for measuring deformation on volcanoes and other natural terrains using InSAR persistent scatterers. *Geophysical Research Letters*, 31, 23. doi:10.1029/2004GL021737

Hu, J., *et al*., 2012. 3D coseismic displacement of 2010 Darfield, New Zealand earthquake estimated from multi-aperture InSAR and D-InSAR measurements. *Journal of Geodesy*, 86 (11), 1029–1041. doi:10.1007/s00190-012-0563-6

Jiang, M., *et al*., 2015. Fast statistically homogeneous pixel selection for covariance matrix estimation for multitemporal InSAR. *IEEE Transactions on Geoscience and Remote Sensing*, 53 (3), 1213–1224. doi:10.1109/TGRS.2014.2336237

Jolivet, R., *et al*., 2014. Improving InSAR geodesy using global atmospheric models. *Journal of Geophysical Research: Solid Earth*, 119 (3), 2324–2341.

Kampes, B.M., 2006. *Radar interferometry: persistent scatterer technique*. Dordrecht: Springer.

Kampes, B.M. and Hanssen, R.F., 2004. Ambiguity resolution for permanent scatterer interferometry. *IEEE Transactions on Geoscience and Remote Sensing*, 42 (11), 2446–2453. doi:10.1109/TGRS.2004.835222

Lanari, R., *et al*., 2004. A small-baseline approach for investigating deformations on full-resolution differential SAR interferograms. *IEEE Transactions on Geoscience and Remote Sensing*, 42 (7), 1377–1386. doi:10.1109/TGRS.2004.828196

Lauknes, T.R., Zebker, H.A., and Larsen, Y., 2011. InSAR deformation time series using an-norm small-baseline approach. *IEEE Transactions on Geoscience and Remote Sensing*, 49 (1), 536–546. doi:10.1109/TGRS.2010.2051951

Li, Z., *et al*., 2005. Interferometric synthetic aperture radar (InSAR) atmospheric correction: GPS, moderate resolution imaging spectroradiometer (MODIS), and InSAR integration. *Journal of Geophysical Research: Solid Earth*, 110 (B03410). doi:10.1029/2004JB003446

Lu, Z. and Dzurisin, D., 2014, *InSAR imaging of Aleutian volcanoes: monitoring a volcanic arc from space*. Berlin: Springer.

Lu, Z., *et al*., 2010. Ground surface deformation patterns, magma supply, and magma storage at Okmok volcano, Alaska, from InSAR analysis: 1. Interruption deformation, 1997–2008. *Journal of Geophysical Research: Solid Earth*, 115 (B00B02). doi:10.1029/2009JB006969

Massonnet, D., *et al*., 1994. Radar interferometric mapping of deformation in the year after the Landers earthquake. *Nature*, 369 (6477), 227–230. doi:10.1038/369227a0

Mora, O., Mallorqui, J.J., and Broquetas, A., 2003. Linear and nonlinear terrain deformation maps from a reduced set of interferometric SAR images. *IEEE Transactions on Geoscience and Remote Sensing*, 41 (10), 2243–2253. doi:10.1109/TGRS.2003.814657

Reale, D., *et al*., 2011. Tomographic imaging and monitoring of buildings with very high resolution SAR data. *IEEE Geoscience and Remote Sensing Letters*, 8 (4), 661–665. doi:10.1109/LGRS.2010.2098845

Refice, A., Bovenga, F., and Nutricato, R., 2006. MST-based stepwise connection strategies for multipass radar data, with application to coregistration and equalization. *IEEE Transactions on Geoscience and Remote Sensing*, 44 (8), 2029–2040. doi:10.1109/TGRS.2006.872907

Remy, D., *et al*., 2003. Accurate measurements of tropospheric effects in volcanic areas from SAR interferometry data: application to Sakurajima volcano (Japan). *Earth and Planetary Science Letters*, 213 (3–4), 299–310. doi:10.1016/S0012-821X(03)00331-5

Samsonov, S., Van Derkooij, M., and Tiampo, K., 2011. A simultaneous inversion for deformation rates and topographic errors of DInSAR data utilizing linear least square inversion technique. *Computers & Geosciences*, 37 (8), 1083–1091. doi:10.1016/j.cageo.2011.01.007

Schmidt, D. A. and Bürgmann, R., 2003. Time-dependent land uplift and subsidence in the Santa Clara valley, California, from a large interferometric synthetic aperture radar data set. *Journal of Geophysical Research: Solid Earth*, 108 (B9), 2146.

Shanker, P. and Zebker, H., 2007. Persistent scatterer selection using maximum likelihood estimation. *Geophysical Research Letters*, 34 (22), 2–5. doi:10.1029/2007GL030806

Simons, M., Fialko, Y., and Rivera, L., 2002. Coseismic deformation from the 1999 Mw 7.1 Hector Mine, California, earthquake as inferred from InSAR and GPS observations. *Bulletin of the Seismological Society of America*, 92 (4), 1390–1402. doi:10.1785/0120000933

Sousa, J.J., *et al*., 2011. Persistent scatterer InSAR: a comparison of methodologies based on a model of temporal deformation vs. spatial correlation selection criteria. *Remote Sensing of Environment*, 115 (10), 2652–2663. doi:10.1016/j.rse.2011.05.021

Sun, Q., *et al*., 2015. Slope deformation prior to Zhouqu, China landslide from InSAR time series analysis. *Remote Sensing of Environment*, 156, 45–57. doi:10.1016/j.rse.2014.09.029

Thiele, A., *et al*., 2007. Building recognition from multi-aspect high-resolution InSAR data in urban areas. *IEEE Transactions on Geoscience and Remote Sensing*, 45 (11), 3583–3593. doi:10.1109/TGRS.2007.898440

Usai, S., 2003. A least squares database approach for SAR interferometric data. *IEEE Transactions on Geoscience and Remote Sensing*, 41 (4), 753–760. doi:10.1109/TGRS.2003.810675

Usai, S. and Hanssen, R., 1997. Long time scale INSAR by means of high coherence features. *European Space Agency-Publications-Esa Sp*, 414, 225–228.

Wang, H., *et al*., 2012. InSAR reveals coastal subsidence in the Pearl River Delta, China. *Geophysics Journal International*, 191, 1119–1128.

Werner, C., *et al*., 2003. Interferometric point target analysis for deformation mapping, in International Geoscience and Remote Sensing Symposium, IGARSS'03, pp. 4362–4364.

Zebker, H.A. and Chen, K., 2005. Accurate estimation of correlation in InSAR observations. *IEEE Geoscience and Remote Sensing Letters*, 2 (2), 124–127. doi:10.1109/LGRS.2004.842375

Zebker, H.A., Rosen, P.A., and Hensley, S., 1997. Atmospheric effects in interferometric synthetic aperture radar surface deformation and topographic maps. *Journal of Geophysical Research: Solid Earth (1978–2012)*, 102 (B4), 7547–7563.

Zebker, H.A. and Villasenor, J., 1992. Decorrelation in interferometric radar echoes. *IEEE Transactions on Geoscience and Remote Sensing*, 30 (5), 950–959. doi:10.1109/36.175330

Zhang, L., Ding, X.L., and Lu, Z., 2011. Modeling PSInSAR time series without phase unwrapping. *IEEE Transactions on Geoscience and Remote Sensing*, 49 (1), 547–556. doi:10.1109/TGRS.2010.2052625

Zhang, L., *et al*., 2014. A novel multi-temporal InSAR model for joint estimation of deformation rates and orbital errors. *IEEE Transactions on Geoscience and Remote Sensing*, 52 (6), 3529–3540. doi:10.1109/TGRS.2013.2273374

Zhang, L., *et al*., 2012. Mapping ground surface deformation using temporarily coherent point SAR interferometry: application to Los Angeles Basin. *Remote Sensing of Environment*, 117, 429–439. doi:10.1016/j.rse.2011.10.020

Zhao, C.Y., *et al*., 2012. Large area landslide detection and monitoring with ALOS/PALSAR imagery data over Northern California and Southern Oregon, USA. *Remote Sensing of Environment*, 124, 348–359. doi:10.1016/j.rse.2012.05.025